Supplemental material for: **Structural origins of dielectric anomalies in the filled tetragonal tungsten bronze, $Sr_2NaNb_5O_{15}$**

Jeremiah P. Tidey,[1] Urmimala Dey,[2] Ana M. Sanchez,[1] Wei-Tin Chen,[3,4] Bo-Hao Chen,[5] Yu-Chun Chuang,[5] Maria T. Fernandez-Diaz,[6] Nicholas Bristowe,[2] Richard Beanland[1], Mark S. Senn[7]

1) Department of Physics, University of Warwick, Gibbet Hill Road, Coventry, CV4 7AL
2) Centre for Materials Physics, Durham University, South Road, Durham DH1 3LE, United Kingdom
3) Center for Condensed Matter Sciences and Center of Atomic Initiative for New Materials, National Taiwan University, Taipei 10617, Taiwan
4) Taiwan Consortium of Emergent Crystalline Materials, National Science and Technology Council, Taipei 10622, Taiwan
5) National Synchrotron Radiation Research Center, Hsinchu 30076, Taiwan
6) Institut Laue-Langevin, BP 156X, Grenoble F-38042, France
7) Department of Chemistry, University of Warwick, Gibbet Hill Road, Coventry, CV4 7AL

Section A: Additional tables and figures

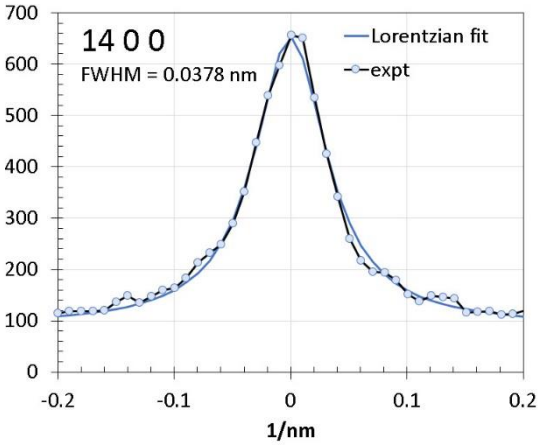

Figure SI1. As a representative example of a diffraction spot some distance from the direct 000 beam, we show the intensity profile of the **g** = 14 0 0_{tet} spot ($|\mathbf{g}|$ = 11.336 nm^{-1}) in the SAED pattern of Figure 2(a), fitted with a Lorentzian function. Peak broadening is consistent with being entirely instrumental with a full width at half-maximum (FWHM) of 0.0378 nm^{-1}. Similar values were found across the SAED pattern, irrespective of the direction or magnitude of **g**-vector. For this reflection, the measurement places an upper limit on strain in the material at 0.0378/11.336 = 0.3%.

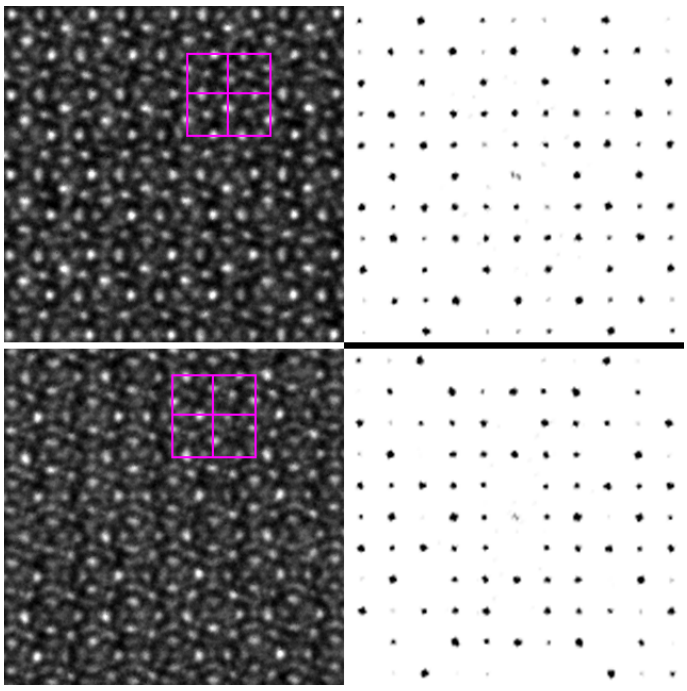

Figure SI2. Fourier transforms of the HREM image in the two different domains showing systematic absences in the horizontal axis for periodicity doubled vertically (top), and vice-versa (bottom). Structural units are highlighted with magenta squares. The FFTs of the 2D images, equating slices through *hk*0, contain systematic absences indicative of further symmetry, rotated 90 degrees between the two.

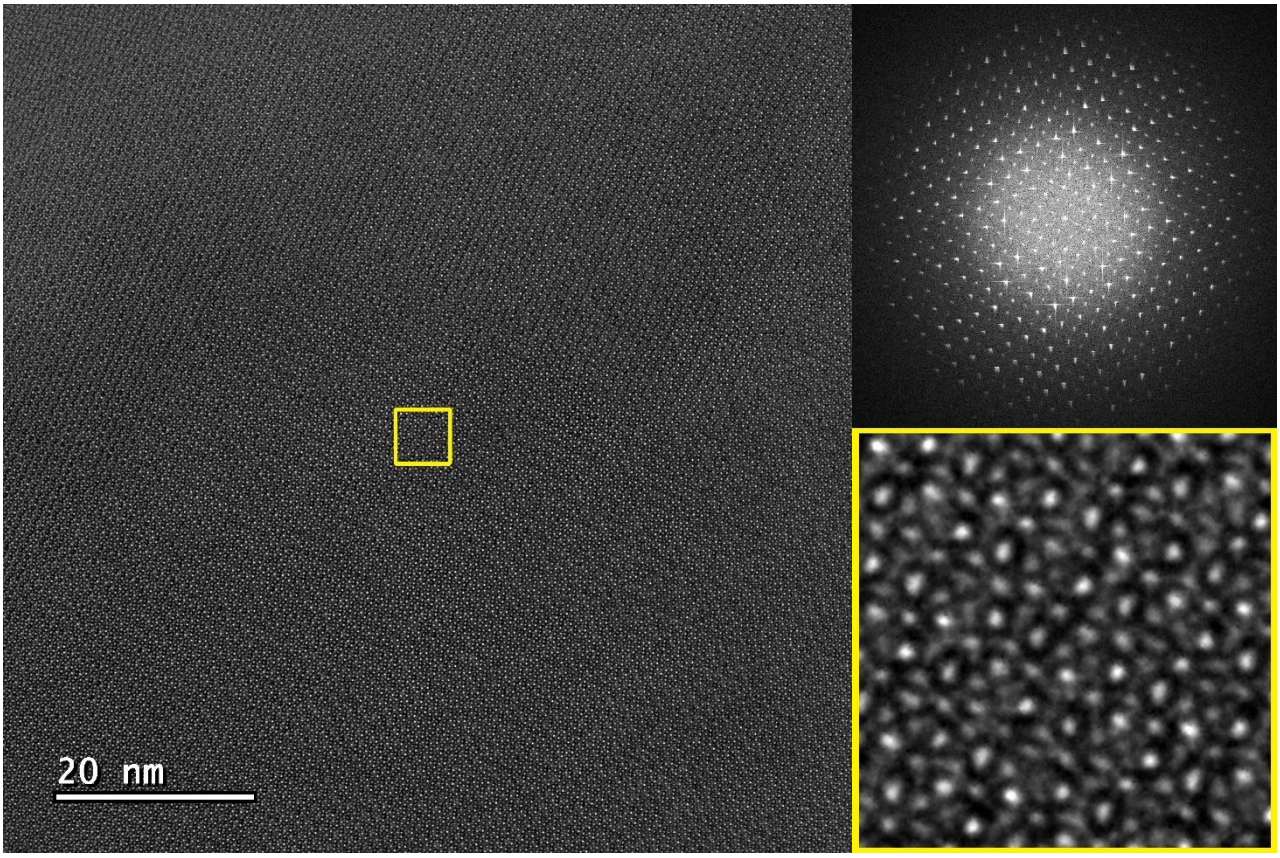

Figure SI3. The raw image for Figure 2(b) and its Fourier transform. An enlargement of the area highlighted in yellow is also shown. Most of the image is taken up with a domain with doubling along the vertical axis, while the top and right of the image has doubling along a horizontal axis.

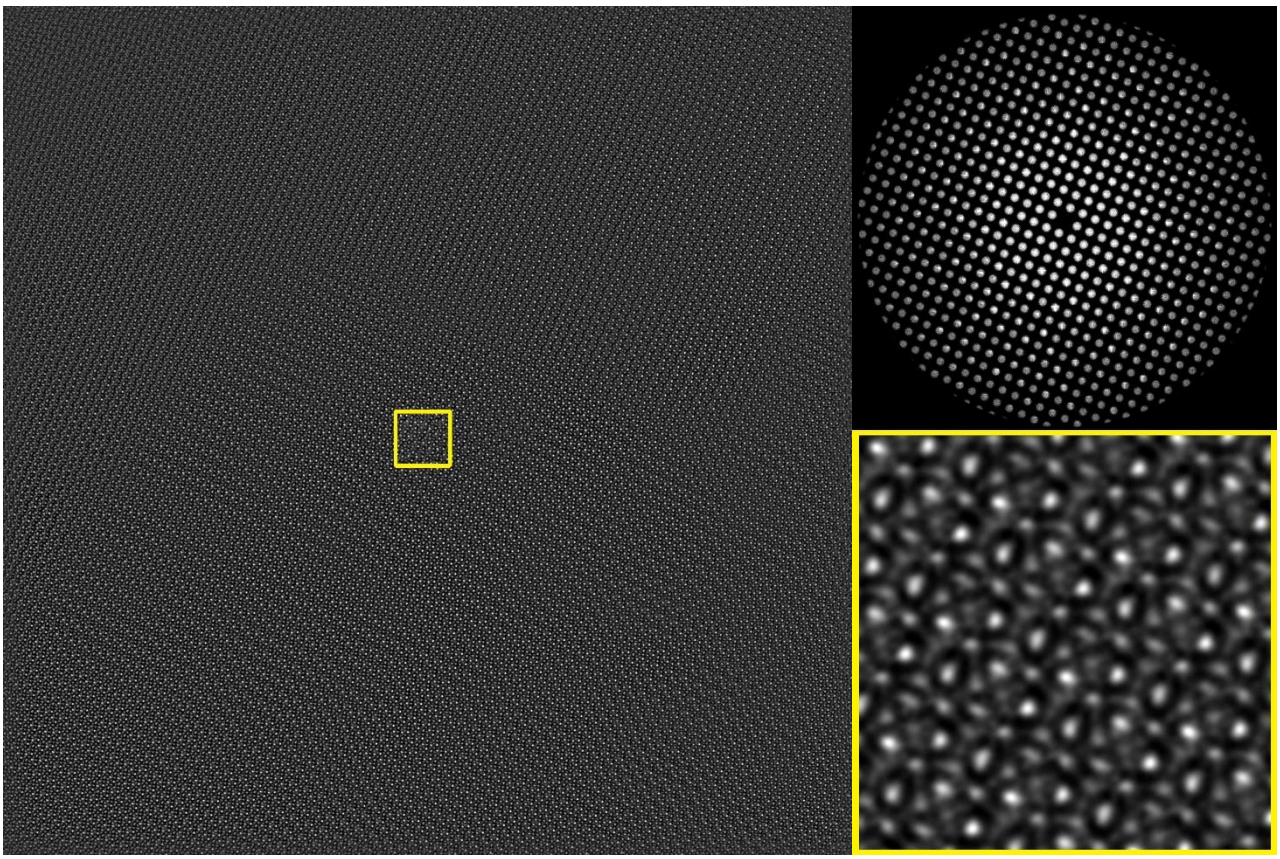

Figure SI4 Applying a Bragg filter to the Fourier transform reduces noise and flattens background contrast. Note the lack of any real change to the features of the pattern.

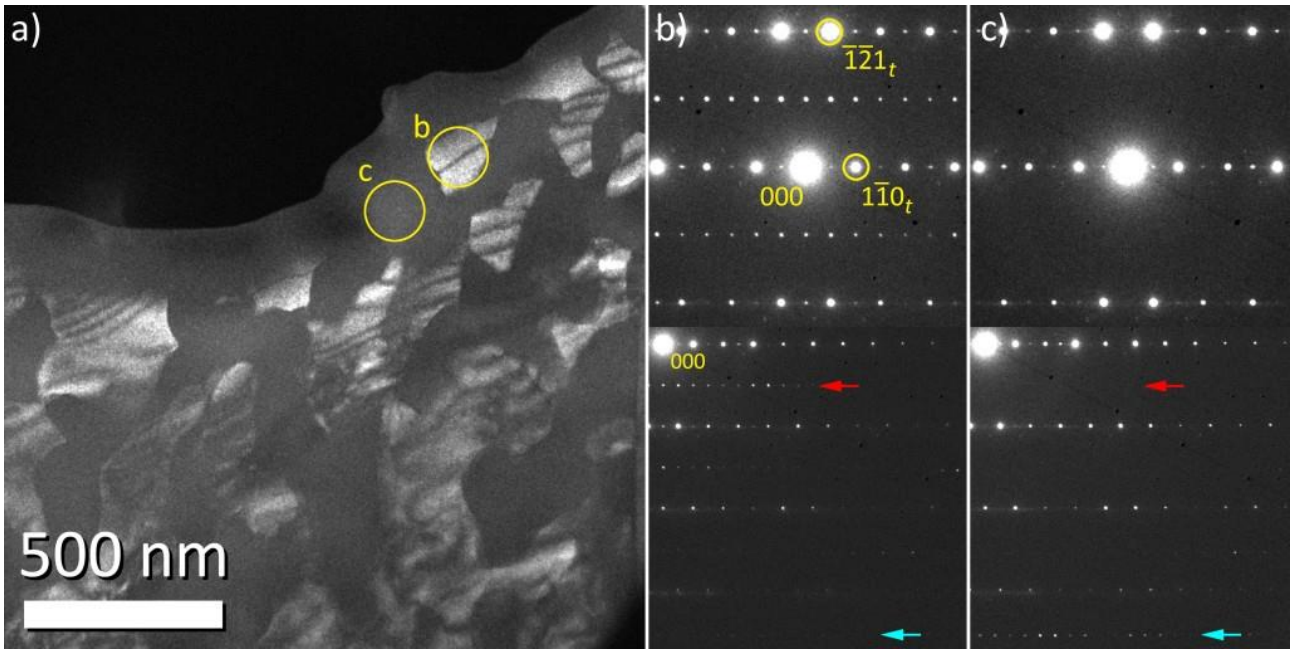

Figure SI5. (a) Dark field imaging and (b) - (c) SAED patterns taken from a SNN crystal at the [113] zone axis, showing complementary behaviour of ZOLZ and FOLZ superstructure spots similar to the [110] data in Figure 2(c-e). Dark stripes in the diffracting domains in (a) arise from antiphase boundaries.

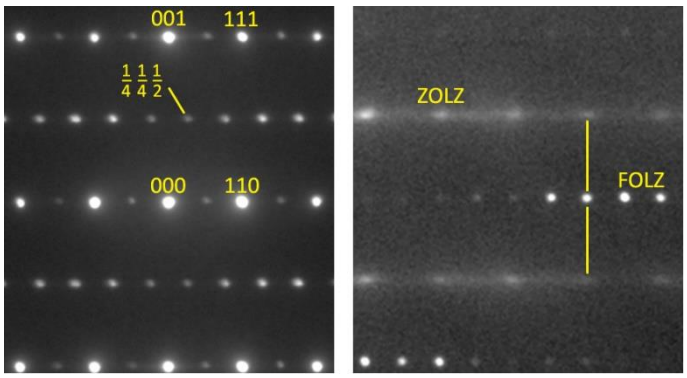

Figure SI6. Enlargements of Figure 2 (d) and (e) showing the position of superstructure spots.

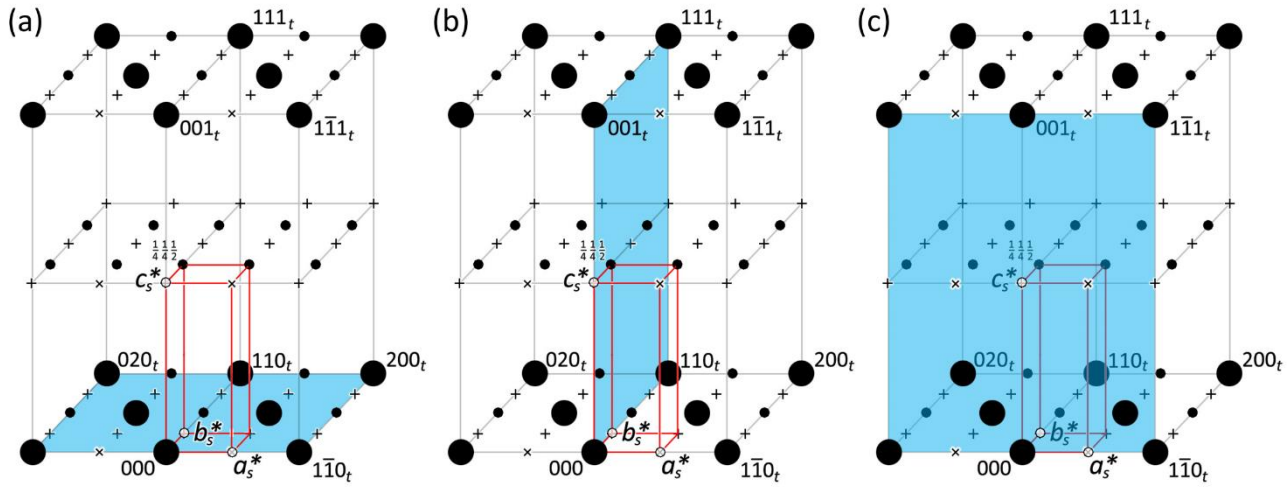

Figure SI7. Sections through reciprocal space highlighted in blue, corresponding to the ZOLZ of SAED patterns in Figures (a) 2(a), (b) 2(d) and (c) 2(e). Indexing is according to the tetragonal aristotype cell. Large circles = aristotype reflections; small circles = superstructure reflections; x,+ = systematic absences due to *a*-glide and A-centring, respectively; principal reciprocal lattice vectors of the supercell are marked a_s^*, b_s^*, c_s^*; red cuboid indicates reciprocal supercell; grey lines added to guide the eyes.

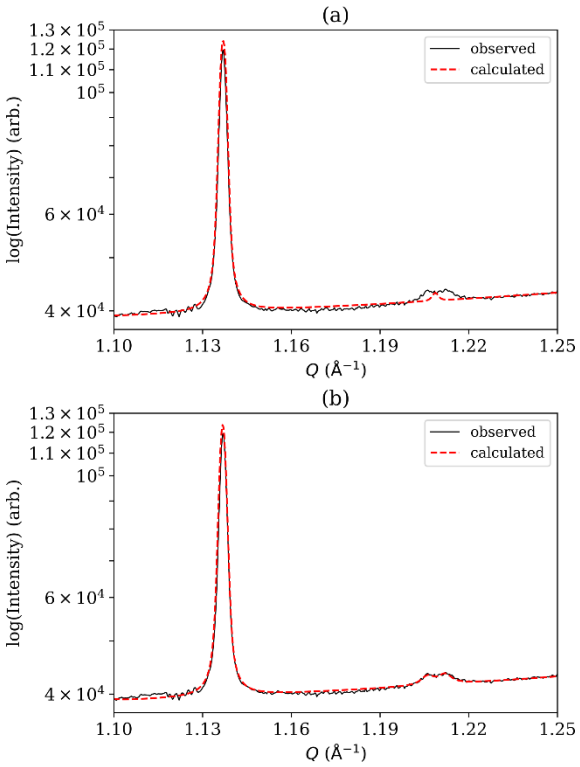

Figure SI8: Fit traces of Rietveld refinements to high-resolution powder X-ray diffraction data from Diamond Light Source showing representative commensurate (Q = 1.135) and incommensurate (Q = 1.20-1.22) intensities. (a) A commensurate refinement in *Ama*2. (b) Incommensurate Pawley refinement in *Cmm*2 (basis = {(1,−1,0),(1,1,0),(0,0,1)}) using first-index $\mathbf{k}_i$ satellite peaks only.

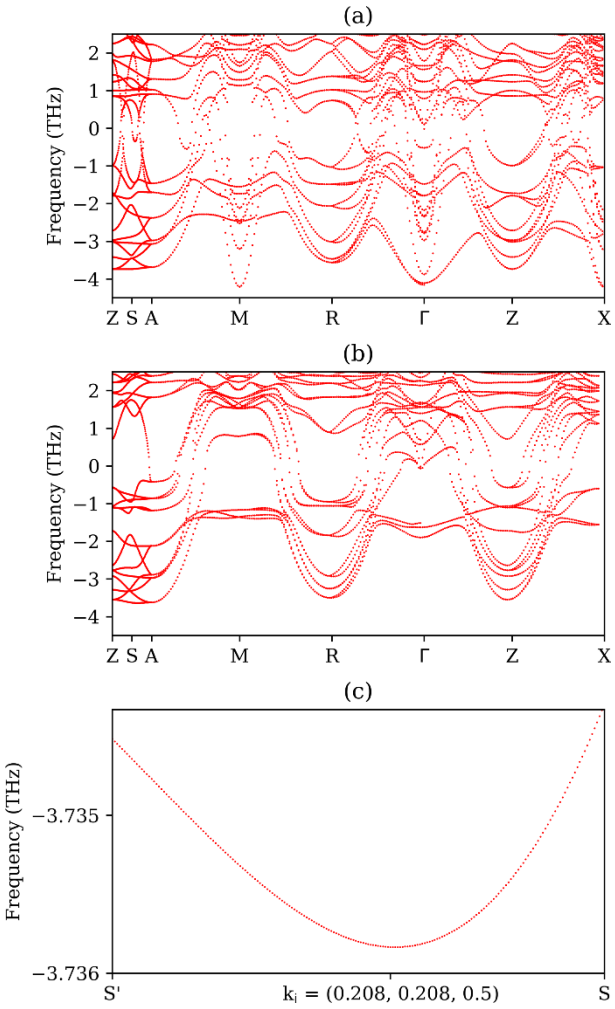

Figure SI9: Phonon spectra calculated for the (a) aristotype *P*4/*mbm* and (b) polar *P*4*bm* structures. Negative phonon frequencies represent unstable phonon modes. (c) shows the lowest frequency phonon band along the S' (0.15, 0.15, ½) – S (¼, ¼, ½) direction in the *P*4/*mbm* phase. Presence of a dip near the S-point indicates the incommensurate nature of the SNN structure associated with the tilt distortion. $\mathbf{k}_i$ denotes the incommensurate modulation vector obtained from DFT calculations on a $\sqrt{2}\times\sqrt{2}\times4$ phonon supercell**.**

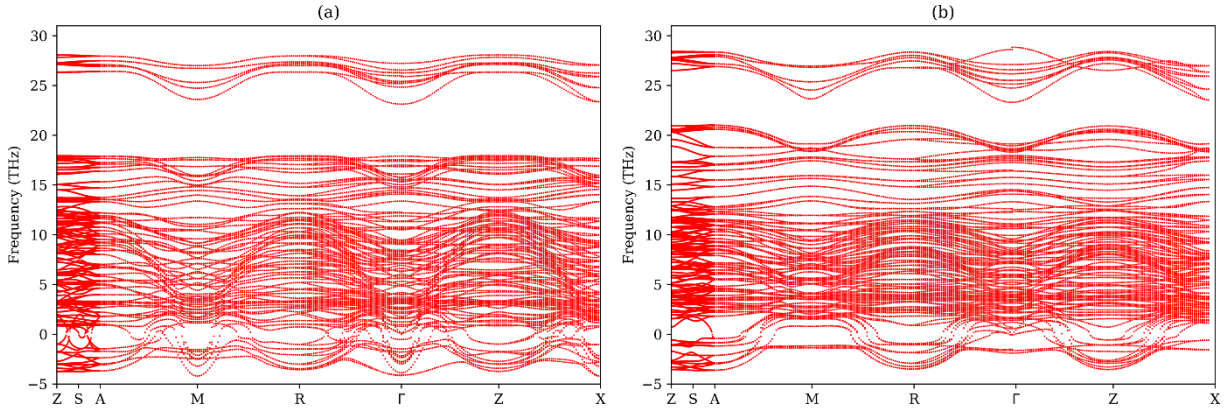

Figure SI0 Phonon spectra calculated for the (a) aristotype *P*4/*mbm* and (b) polar *P*4*bm* structures. Negative phonon frequencies represent unstable phonon modes.

Table SI1. Comparison between experimental room-temperature and DFT-calculated *Ama*2 structures. Numbers in square parentheses constrained to zero in our refinement.

Structural parameters	Experimental values (Ap)	DFT-optimized values

Lattice constants (Å)	a = 17.48480(10) b = 34.92518(19) c = 7.78510(2)	a = 17.45040 b = 34.82551 c = 7.80878
Cell angles (°)	α = 90 β = 90 γ = 90	α = 90 β = 90 γ = 90
Volume (Å^3)	4754.05(4)	4745.54
Irrep (OPD) amplitudes with respect to *P4/mbm* parent (Å)	$\Gamma_1^+(a)$: 0.5667 $\Gamma_4^+(a)$: 0.1095 $\Gamma_2^-(a)$: 0.0012 $\Gamma_3^-(a)$: 0.4748 $M_5^+(a,a)$: [0] $M_5^-(a,a)$: [0] $S_1(a,0;0,0)$: [0] $S_3(a,0;0,0)$: 2.0593	$\Gamma_1^+(a)$: 0.5553 $\Gamma_4^+(a)$: 0.4104 $\Gamma_2^-(a)$: 0.0876 $\Gamma_3^-(a)$: 0.8499 $M_5^+(a,a)$: 0.2684 $M_5^-(a,a)$: 0.1362 $S_1(a,0;0,0)$: 0.3661 $S_3(a,0;0,0)$: 2.3440

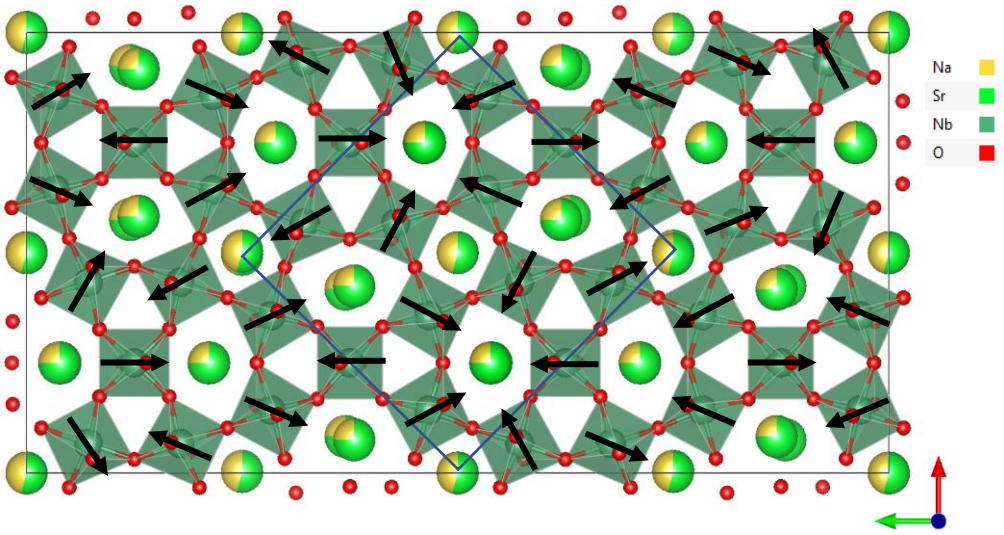

Figure SI11. Depiction of the refined S_3 tilt system showing the movement of top-most apical oxygens as the NbO_6 octahedra rotate about their centre. Competitive refinement of the Na:Sr site occupancy as an average across all crystallographically inequivalent sites yielded ratios of 0.48:0.52 at *A*1 sites and 0.26:0.74 at *A*2, indicated here as proportional segments of those sites, in agreement with the findings of García-González *et al*. [0.45:0.55 and 0.31:0.69, respectively].[1] Surprisingly, given the atomic radii of the cations and sterics the relevant sites, peaks in residual electron density difference maps suggest limited filling of the *C* sites. Their stable refinement proves beyond the reach of our PXRD experiment, but the phenomenon is clearly confirmed by atomic resolution STEM (Figure SI12) along with the existence of vacancies at the *A*-sites (Figure SI13). Zhu *et al*. speculate that *A*1 vacancies allow the strained tilt network of the incommensurate phase to relax, giving the predominantly commensurate modulations found across the series $Ba_4RE_{0.67}|\_|_{1.33}Nb_{10}O_{30}$ (RE = La, Nd, Sm, Gd, Y; and |_| denoting vacancies).[2] There may then exist a driving force for the occupation of the smaller *C*-site in a concomitant relaxation of the tilt system. We also note the existence of structured diffuse scattering, perpendicular to [001] at $l_{tet} = n$ (see lower parts of Figure 2(d) and 2(e)). Since these appear to consist planes in reciprocal space, we identify there to be rods of correlated disorder parallel to the *c*-axis in the real structure which maintain the aristotypical periodicity of this axis. Two probable sources for this can readily be envisaged: a preference to equal occupation of neighbouring *A*-sites along *c*; or the coherence of the polar Γ_3^- distortions within but not between perovskite- and/or *A*-site columns, as shown by Krayzman *et al*. in the case of $Sr_{0.61}Ba_{0.39}Nb_2O_6$.[3]

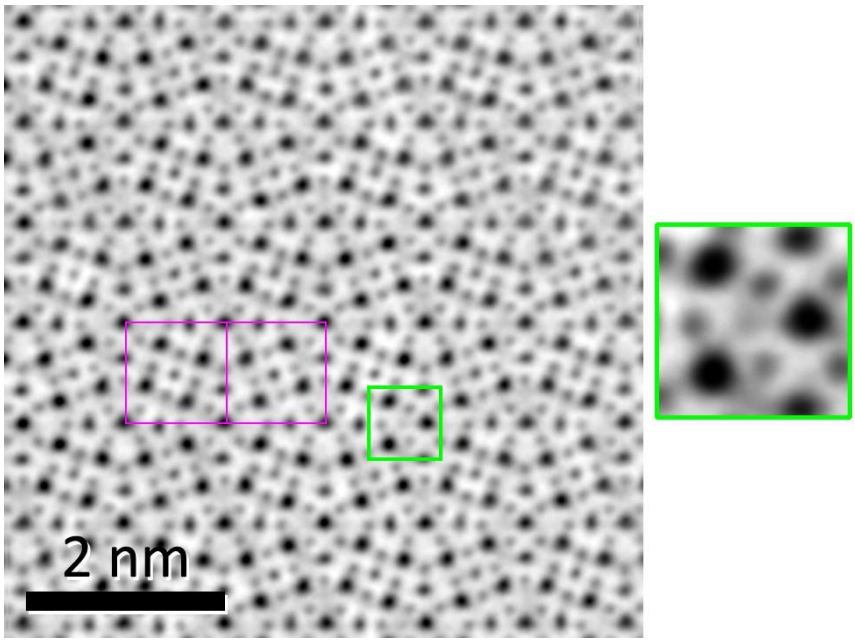

Figure SI12. Annular bright-field (ABF)-STEM image taken along the c-axis. Structural units corresponding to Figure 1(a) are highlighted by magenta boxes. The green box highlights dark contrast at a triangular *C*-type site, indicating a non-zero occupancy. While most *C*-sites do not show any contrast, other examples can be found with careful inspection.

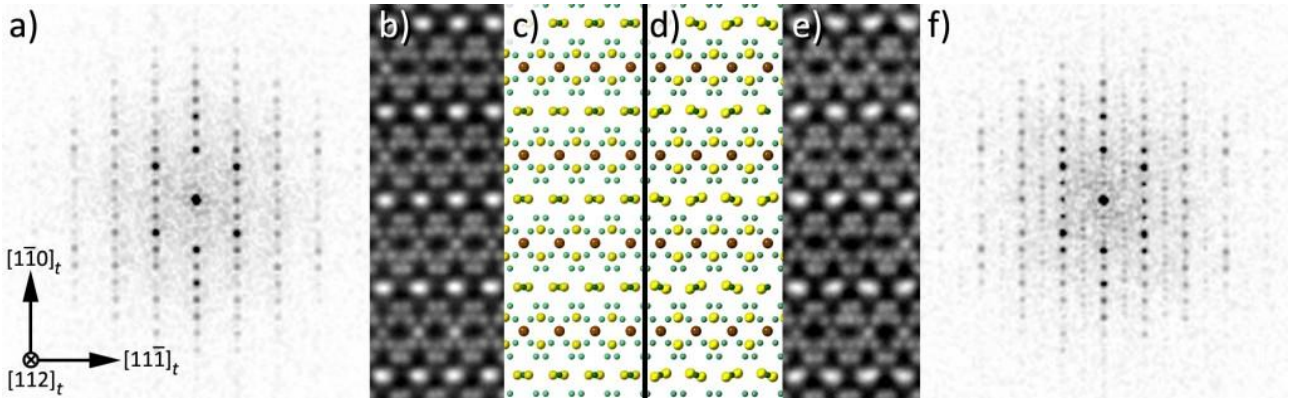

Figure SI13: ADF-STEM imaging at the $[112]_{tet}$ zone axis. Different regions can be identified by their Fourier transforms (a, b) without superstructure spots and (e, f) with superstructure spots, corresponding to different merohedral twins as shown in Figure 2(c-e) and Figure SI5. The main difference in the structure is the displacement of the *A*2 Sr/Na sites, yellow atoms in the tetragonal aristotype (c) and the *Ama*2 structure (d). (*A*1 sites = brown, *B* sites = green.) The ADF-STEM images are 1.3 nm wide, with a height of two aristotype lattice periods; full images are shown in Figure SI14.

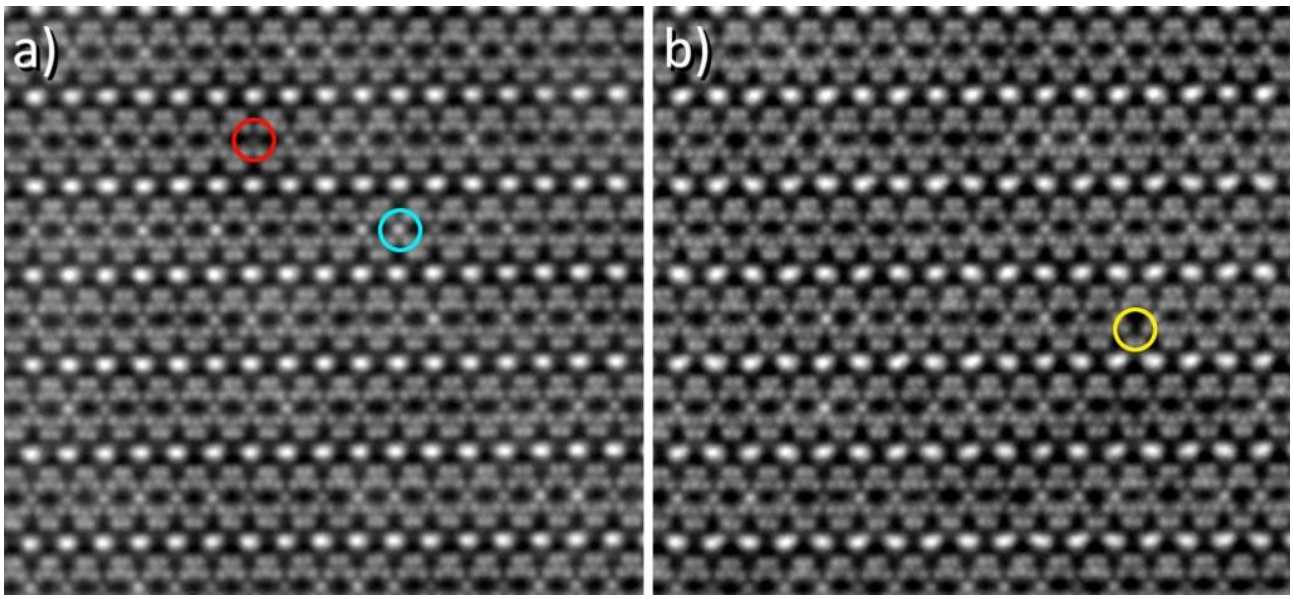

Figure SI14. Larger ADF-STEM images corresponding to Figure SI13. As well as the difference in the shape of the brightest *A*2+*B*-site atom columns, other types of cation disorder are visible including varying occupancy, revealed by different contrast at *A*1 sites (red and cyan circles) and *A*2 vacancies (yellow circle). The varying contrast is visible for this projection since spacing of atoms along the electron beam in all the less intense columns is relatively large at 0.96 nm, meaning that in a specimen of ~10nm in thickness, as shown here, there are only ~10 atoms in each column. Since contrast of the atom columns is dependent upon mean atomic number, statistical variations due to varying populations of Sr (Z = 38) and Na (Z = 11) on the *A*-sites can thus produce a large change in relative intensity. In this projection, C-sites are either (i) adjacent to the strong contrast of the *A*2+*B* sites, or (ii) adjacent to the yellow-circled *A*2 site.

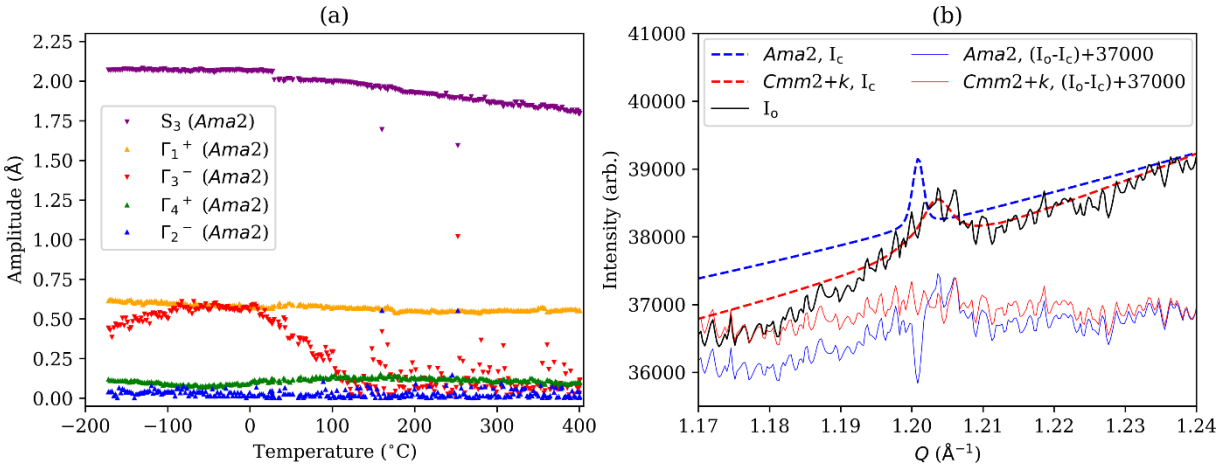

Figure SI15. Plots of: (a) the refined distortion modes from our model in the *Ama*2 commensurate approximation, including those two temperatures omitted from the main manuscript where poor conditioning of the least squares matrix and overlap of peaks with impurity phase resulted in the refinement adopting false minima; (b) plot of the refinement fit of a ~[¼,¼,½] superstructure reflection at 627 °C for the commensurate *Ama*2 and incommensurate *Cmm*2+*k* models, showing the sample to remain incommensurately modulated at the maximum temperatures we study.

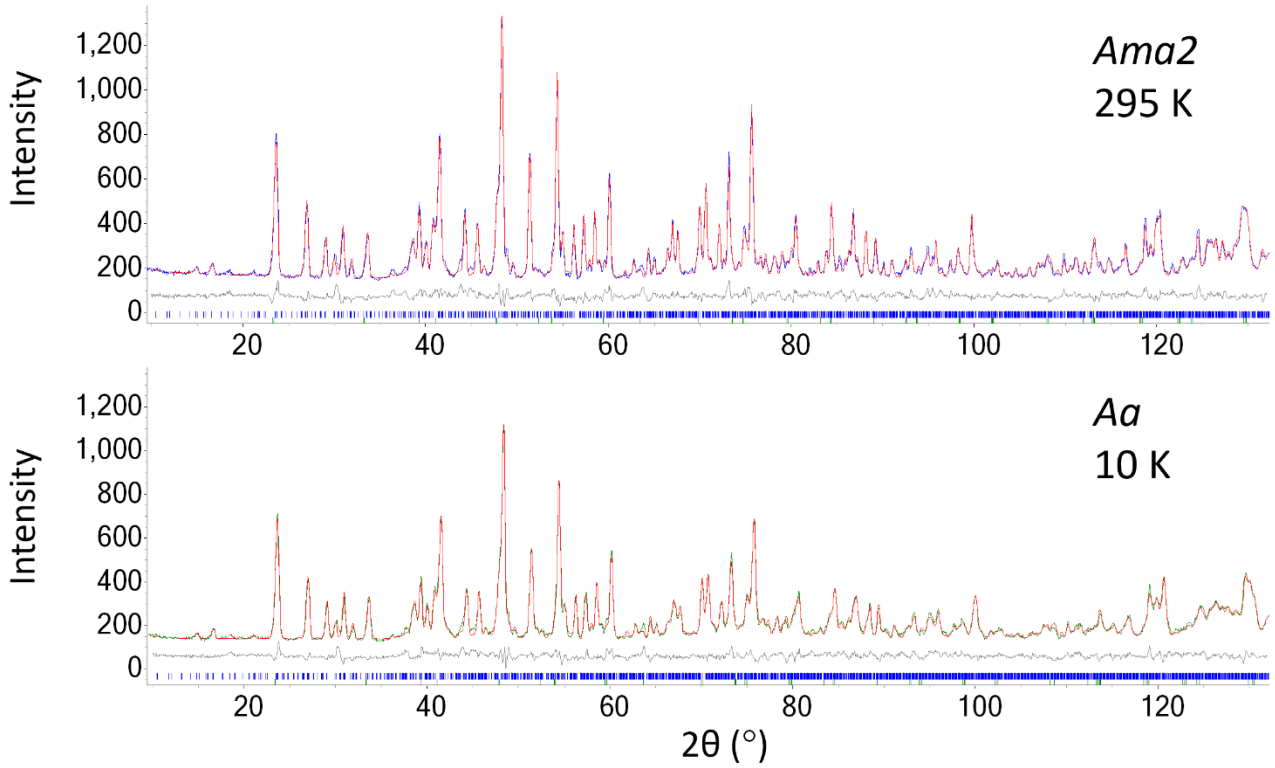

Figure SI16. Plot of neutron powder traces for the Ama2 and Aa phase at 298 and 10 K, respectively.

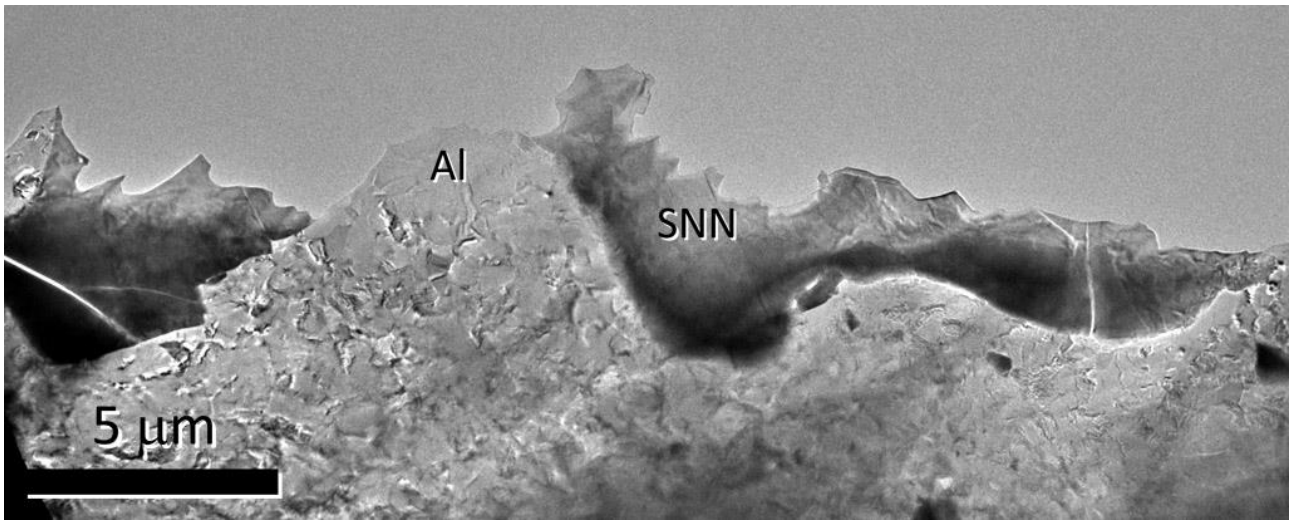

Figure SI17. Bright field TEM image showing the edge of the specimen with SNN grains held in the Al matrix. After cold rolling the Al forms a continuous matrix with embedded ceramic particles. At the edges of the ion-milled hole in the specimen, extensive regions of material with thicknesses down to only a few nm can be found. The TEM specimens produced here contain extensive regions of material tens of nm in thickness, allowing individual grains to be examined in detail. The SNN powder consisted of grains from 0.5 – 10 µm in size that appeared relatively featureless in bright field images, with no dislocations, planar defects, twins or ferroelastic domain walls visible. However, under some diffraction conditions, faint domain contrast could be seen as brighter and darker patches, roughly 100 nm in size, with curved boundaries (Figure SI18). No strain contrast was observed at these boundaries, indicating an essentially contiguous crystal.

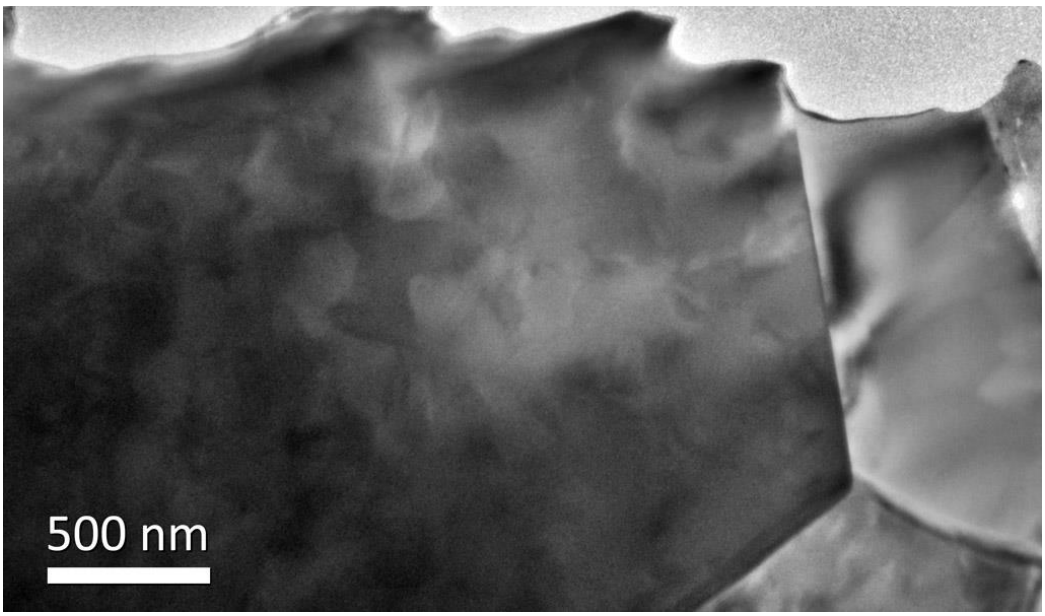

Figure SI18. Bright field TEM image of a SNN grain close to [001] orientation, with domains of different contrast and curved boundaries faintly visible.

Section B: Density functional theory

DFT calculations further support the assignment of an *Ama*2/*Amam* phase transition in the commensurate approximation. In Table 1 of the main manuscript (recreated as Table SI2 for convenience), we list the relative energies of the subgroup structures obtained by condensing in different unstable phonon modes in the aristotype phase. As seen, the nominal *Ama*2 structure is obtained from the condensation of Γ_3^- and S_3 modes with an energy of ~−1.50 eV compared to the aristotype. Individually condensing in those modes instead constitutes energies of −0.20 and −1.36 eV in space groups *P*4*bm* (basis = {(1,0,0), (0,1,0), (0,0,1)}) and *Amam* (basis = {(1,−1,0), (2,2,0), (0,0,2)}, origin shift=(½,0,0)), respectively. Thus, it might be expected that the S_3 distortion arises first as the aristotype is cooled, with the ferroelastic *P*4/*mbm*→*Amam* phase transition at temperatures above those we investigate. Further cooling would result in the Γ_3^- mode subsequently softening to give the ferroelectric *Amam*→*Ama*2 phase transition we observe in the commensurate approximation. This sequence of energy lowering is opposite to the case of BNN,[4] where the polar mode lowers the energy more compared to the tilt mode. This opposite trend is expected in SNN as the presence of smaller Sr^{2+} ions can lead to larger tilting of the NbO_6 octahedra, compared to that in the Ba variant.

Table SI2: Space groups, lattice parameters, and relative energies of child structures obtained by the condensation of unstable phonon modes in the parent *P*4/*mbm* phase. Relative energy values for BNN are taken from Ref. [4].

	SNN				BNN[4]
Space group (Condensed irreps)	***a* (Å)**	***b* (Å)**	***c* (Å)**	**Relative energy per 46-atom unit cell (eV)**	**Relative energy per 46-atom unit cell (eV)**
*P*4/*mbm*	12.470	12.470	3.939	0.00	0.00
*P*4*bm* ($\Gamma_3^-(a)$)	12.437	12.437	3.996	−0.20	−0.41
Amam ($S_3(0,0;a,0)$)	17.507	35.117	7.674	−1.36	-
*Ama*2 ($\Gamma_3^-(a) \oplus S_3(a,0;0,0)$)	17.450	34.826	7.809	−1.50	−0.54
Aa ($\Gamma_3^-(a) \oplus \Gamma_5^-(a,a) \oplus S_3(a,0;0,0)$)	17.615	34.828	7.752	−1.63	-

Computation of the mode amplitudes with respect to the aristotype phase further corroborates our experimental data. The amplitude of the S_3 mode increases slightly from 4.671 Å in the *Amam* phase to 4.688 Å in the *Ama*2 phase, consistent with the trends in Figure 3(d) and SI15(a). On the other hand, the S_1 mode, which is absent in the *Amam* phase, develops a very small value of 0.732 Å in the *Ama*2 structure. Similarly, amplitudes of the polar mode Γ_3^- and piezoelectric mode Γ_2^- distortions are identically both zero in the nonpolar *Amam* structure. The polar mode then develops a large value amplitude (1.700 Å) in the *Ama*2 phase together with a very small piezoelectric mode (0.175 Å), as observed in the variable temperature PSD data (Figure 3(d) and SI15(a)). This is in contrast to the work of Krayzman *et al.* who find competition between these in their investigation of the unfilled TTB, $Sr_{0.31}Ba_{0.69}Nb_2O_6$ (SBN).[3]

The variable temperature PSD data in Figure 3(a-b) show three distinct regions in the lattice parameter gradients which can also be rationalised by DFT. We find that the *c*-lattice parameter is increased in the relaxed *Ama*2 phase, compared to that for *Amam*, alongside a decrease in the *a* and *b* lattice parameters, much as is captured in the PXRD. This can be explained by coupling of the polarization and (out-of-plane)-strain in the *Ama*2 structure, which expands the cell along the *c*-direction with contraction along *a* and *b*. Given the ferroelectric mode only becomes finite in the *Ama*2 phase, we assign T_2 as the ferroelectric transition temperature associated with the softening of the Γ_3^- mode, which coincides with the *Amam*/*Ama*2 structural phase transition, providing further support to the experimental findings.

While we initially obtain the *Ama*2 phase by subsequently condensing in the $\Gamma_3^-(a)$ and $S_3(a,0;0,0)$ modes from a relaxed aristotype phase, the structure nevertheless comprises six displacive and two strain modes (Table SI1). Analysis using INVARIANTS[7,8] reveal that there are six other binary combinations of irreps which can lead to the same structure. In order to elucidate the primary order parameters (POPs), we individually freeze in the separate modes in the *P*4/*mbm* phase and calculate the energy lowering corresponding to each of the resulting structures, reported in this table. In Table SI3, it is found that $S_3(a,0;0,0)$ contributes to the largest energy lowering from the *P*4/*mbm* phase, followed by $M_5^+(a,a)$ and $\Gamma_3^-(a)$. However, there is no binary combination of modes leading to the *Ama*2 structure which involves $M_5^+(a,a)$ as a POP. Therefore, by comparing the contributions of the individual modes to energy lowering, we predict that $\Gamma_3^-(a)$ and $S_3(a,0;0,0)$ are most likely the POPs that drive the phase transition from the aristotype *P*4/*mbm* structure to the room temperature phase, supporting the experimental findings. We note that our zero Kelvin calculations lead to higher amplitudes of the modes compared to the experimental amplitudes (Table SI1, SI4-5), which can be attributed to the thermal fluctuations at room temperature and the highly under-constrained nature of the experimental model.

Table SI3. Space groups and relative energies of resulting structures obtained by condensation into the parent *P*4*/mbm* structure of the individual displacive irreps allowed in the commensurate *Ama*2 phase. We note that almost all of the below relaxed structures will develop distortions of additional irreps that further contribute to the energy landscape, however, these are omitted for clarity.

Irrep (OPD)	Space group	Cell basis	Relative energy w.r.t. 46-atom aristotype cell (eV)
$\Gamma_2^-(a)$	*P*−42$_1$*m*	{(1,0,0), (0,1,0), (0,0,1)}	−0.10
$\Gamma_3^-(a)$	*P*4*bm*	{(1,0,0), (0,1,0), (0,0,1)}	−0.20
$M_5^+(a,a)$	*Pmma*	{(−1,1,0), (0,0,1), (1,1,0)}	−0.43
$M_5^-(a,a)$	*Pmna*	{(−1,1,0), (0,0,1), (1,1,0)}	−0.10
$S_1(a,0;0,0)$	*Amam*	{(1,1,0), (−2,2,0), (0,0,2)}	−0.06
$S_3(a,0;0,0)$	*Amam*	{(1,1,0), (−2,2,0), (0,0,2)}	−1.36
$\Gamma_2^-(a) \oplus S_1(a,0;0,0)$	*Ama*2	{(1,−1,0), (2,2,0), (0,0,2)}	−1.50
$\Gamma_3^-(a) \oplus S_1(a,0;0,0)$	*Ama*2	{(1,−1,0), (2,2,0), (0,0,2)}	−1.50
$M_5^-(a,a) \oplus S_1(a,0;0,0)$	*Ama*2	{(1,−1,0), (2,2,0), (0,0,2)}	−1.50

$\Gamma_2^-(a) \oplus S_3(a,0;0,0)$	*Ama*2	{(1,−1,0), (2,2,0), (0,0,2)}	−1.50
$\Gamma_3^-(a) \oplus S_3(a,0;0,0)$	*Ama*2	{(1,−1,0), (2,2,0), (0,0,2)}	−1.50
$M_5^-(a,a) \oplus S_3(a,0;0,0)$	*Ama*2	{(1,−1,0), (2,2,0), (0,0,2)}	−1.50
$S_1(a,0;0,0) \oplus S_3(a,0;0,0)$	*Ama*2	{(1,−1,0), (2,2,0), (0,0,2)}	−1.50

Table SI4. Comparison between DFT-calculated *Amam* and high temperature (206 °C) structures, considering only select parameters from our *Ama*2 model (which refines at the presented temperature to an extremely close approximation of the *Amam* symmetry).

Structural parameters	**Experimental values**	**DFT-optimized values**
Lattice constants (Å)	*a* = 17. 52196(9) *b* = 35. 01317(18) *c* = 7. 78204(2)	*a* = 17.50670 *b* = 35.11762 *c* = 7.50670
Cell angles (°)	α = 90 β = 90 γ = 90	α = 90 β = 90 γ = 90
Volume (Å^3)	4774.28(4)	4717.89
Irrep (OPD) amplitudes with respect to *P4/mbm* parent (Å)	$\Gamma_1^+(a)$: 0.5456 $\Gamma_4^+(a)$: 0.1206 $M_5^+(a,-a)$: [0] $S_3(0,0;a,0)$: 1.9281	$\Gamma_1^+(a)$: 0.5536 $\Gamma_4^+(a)$: 0.5222 $M_5^+(a,-a)$: 0.4247 $S_3(0,0;a,0)$: 2.3353

Table SI5. Comparison between DFT-calculated and low temperature experimental (−165 °C) *Aa* structures. Note that we do not consider refinement of the modes in the *Aa* phase to be of as great confidence as in the *Ama*2 model and present these numbers purely for completeness.

Structural parameters	**Experimental values**	**DFT-optimized values**
Lattice constants (Å)	*a* = 17. 48386(7) *b* = 34. 84654(14) *c* = 7. 77562(3)	*a* = 17.61521 *b* = 34.82765 *c* = 7.75204
Cell angles (°)	α = 90 β = 90.0603(8) γ = 90	α = 90 β = 90.3573 γ = 90
Volume (Å^3)	4737.31(3)	4755.761
Irrep (OPD) amplitudes with respect to *P4/mbm* parent (Å)	$\Gamma_1^+(a)$: 0.6183 $\Gamma_4^+(a)$: 0.1242 $\Gamma_5^+(a,-a)$: 0.3258 $\Gamma_2^-(a)$: 0.0579 $\Gamma_3^-(a)$: 0.3863 $\Gamma_5^-(a,a)$: 0.9021 $M_2^+M_3^+(a,b)$: [0] $M_5^+(a,-a)$: [0] $M_1^-M_4^-(a,b)$: [0] $M_5^-(a,-a)$: [0] $S_1(0,0;a,0)$: [0] $S_2(0,0;0,a)$: [0] $S_3(0,0;a,0)$: 2.0603 $S_4(0,0;0,a)$: [0]	$\Gamma_1^+(a)$: 0.5581 $\Gamma_4^+(a)$: 0.1678 $\Gamma_5^+(a,-a)$: 0.0531 $\Gamma_2^-(a)$: 0.0619 $\Gamma_3^-(a)$: 0.5881 $\Gamma_5^-(a,a)$: 0.8905 $M_2^+M_3^+(a,b)$: 0.0299 $M_5^+(a,-a)$: 0.4857 $M_1^-M_4^-(a,b)$: 0.3178 $M_5^-(a,-a)$: 0.1607 $S_1(0,0;a,0)$: 0.2619 $S_2(0,0;0,a)$: 0.1085 $S_3(0,0;a,0)$: 2.2820 $S_4(0,0;0,a)$: 0.4424

DFT prediction of an alternative room temperature phase of SNN

Condensation of the $\Gamma_5^-(a,a)$ mode alone in the *P4/mbm* structure leads to an energy lowering of ~0.68 eV, which is larger than that for the $\Gamma_3^-(a)$ mode shown in Table 1 of the main text. Therefore, without entropic consideration, DFT calculations suggest the presence of an alternative polar orthorhombic phase, *A*2$_1$*am* (basis={(1,1,0), (−2,2,0), (0,0,2)}, origin shift=(½,0,0)), at room temperature which is derived from the combination of irreps $\Gamma_5^-(a,a) \oplus S_3(0,0;a,0)$ and would equally satisfy the results of the electron diffraction and microscopy. However, this result is neither supported by nor adequately explains results from our powder diffraction experiments. Moreover, Γ-phonon calculations in the *Amam* phase shows that the $\Gamma_5^-(a,a)$ mode has much higher frequency compared to the lowest frequency $\Gamma_3^-(a)$ mode. Furthermore, the temperature dependence of lattice parameters and mode amplitudes observed in experiments cannot be explained based on the *A*2$_1$*am* model and, hence, we discard the *A*2$_1$*am* structure for the room temperature phase of SNN.

References

[1] E. Garcıa-Gonzalez, A. Torres-Pardo, R. Jime´nez, J. M. Gonza´lez-Calbet, *Chem. Mater.* **2007**, *19*, 3575.

[2] X. Zhu, M. Fu, M. C. Stennett, P. M. Vilarinho, I. Levin, C. A. Randall, J. Gardner, F. D. Morrison, I. M. Reaney, *Chem. Mater.* **2015**, *27*, 3250.

[3] V. Krayzman, A. Bosak, H. Y. Playford, B. Ravel, I. Levin, *Chem. Mater.* **2022**, *34*, 9989.

[4] S. S. Aamlid, S. M. Selbach, T. Grande, *Inorg. Chem.* **2020**, *59*, 8514.

[5] T. Brown, A. P. Brown, D. A. Hall, T. E. Hooper, Y. Li, S. Micklethwaite, Z. Aslam, S. J. Milne, *J. Eur. Ceram. Soc.* **2021**, *41*, 3416.

[6] S. Xu, R. Hao, Z. Yan, S. Hou, Z. Peng, D. Wu, P. Liang, X. Chao, L. Wei, Z. Yang, *J. Eur. Ceram. Soc.* **2022**, *42*, 2781.

[7] D. M. Hatch, H. T. Stokes, *J. Appl. Crystallogr.* **2003**, *36*, 951.

[8] H. T. Stokes, D. M. Hatch, B. J. Campbell, **n.d.**